=== **SEMICONDUCTORS** ===

Structural and Some Electrophysical Properties of the Solid Solutions $Si_{1-x}Sn_x$ ($0 \leq x \leq 0.04$)

A. S. Saidov[a, *], Sh. N. Usmonov[a, **], M. U. Kalanov[b], A. N. Kurmantayev[c], and A. N. Bahtybayev[c]

[a] Starodubtsev Physical–Technical Institute, Uzbekistan Academy of Sciences,
ul. G. Mavlyanova 2, Tashkent, 700084 Uzbekistan
* e-mail: amin@uzsci.net
** e-mail: sh_usmonov@rambler.ru
[b] Institute of Nuclear Physics, Uzbekistan Academy of Sciences,
Ulugbek, Tashkent, 100214 Uzbekistan
[c] Hoca Ahmet Yesevi International Kazakh-Turkish University,
pl. Esimkhana 2, Turkestan, 487010 Kazakhstan
Received February 7, 2012; in final form, June 24, 2012

Abstract—Films of the solid solutions $Si_{1-x}Sn_x$ ($0 \leq x \leq 0.04$) on Si substrates have been grown by liquid phase epitaxy. The structural features of the films have been investigated using X-ray diffraction. The temperature behavior of current–voltage characteristics and the spectral dependence of the photocurrent for the heterostructures p-Si–n-$Si_{1-x}Sn_x$ ($0 \leq x \leq 0.04$) have been analyzed. The grown epitaxial films of the solid solutions $Si_{1-x}Sn_x$ ($0 \leq x \leq 0.04$) have a perfect single-crystal structure with a (111) orientation and a subgrain size of 60 nm. In the epitaxial films at the Si–SiO_2 interfaces between silicon subgrains and SiO_2 nanocrystals, where there are many sites with a high potential, the Sn ions with a high probability substitute for the Si ions and encourage the formation of Sn nanocrystals with different orientations and, as follows from the analysis of the X-ray diffraction patterns, with different sizes: 8 nm (for the (101) orientation) and 12 nm (for the (200) orientation). The current–voltage characteristics of the heterostructures p-Si–n-$Si_{1-x}Sn_x$ ($0 \leq x \leq 0.04$) are described by the exponential law $J = J_0 \exp(qV/ckT)$ at low voltages ($V < 0.2$ V) and the square law $J = (9q\mu_p\tau_p\mu_n N_d/8d^3)V^2$ at high voltages ($V > 1$ V). These results have been explained by the drift mechanism of charge carrier transport in the electrical resistance relaxation mode.

DOI: 10.1134/S1063783413010290

1. INTRODUCTION

An extension of the spectral range of photosensitivity of semiconductor structures in the infrared region is an important problem of optoelectronics. Devices and instruments operating in the infrared region of the radiation spectrum have been developed on the basis of bulk and epitaxial layers of $Hg_{1-x}Cd_xTe$ solid solutions, silicon Schottky barrier diodes, heterojunctions based on $Si_{1-x}Ge_x$ solid solutions, binary GaSb compounds, $Al_{1-x}Ga_xAs$ heterojunctions, and superlattices of strained layers of $Gd_{1-x}In_xSb$ solid solutions. Among these materials, mercury cadmium telluride $Hg_{1-x}Cd_xTe$ has better fundamental and performance characteristics and can operate at higher temperatures. Consequently, at present, $Hg_{1-x}Cd_xTe$ has mainly been used in infrared radiation detectors. However, it is an expensive material. In this respect, investigation of the possibility of synthesis and photoelectric properties of narrow-band-gap semiconductor solid solutions based on the most studied and available materials, such as Ge, Si, and Sn, is of practical interest. The solid solutions $Ge_{1-x}Sn_x$, $Si_{1-x}Sn_x$, and $Ge_{1-x-y}Si_xSn_y$ have attracted the attention of researchers due to the fact that the presence of an isovalent component of Sn atoms in the crystal lattices of Ge and Si creates favorable conditions for controlling the structural features, photovoltaic and generation–recombination processes, and processes of charge carrier transport in these materials and related structures.

Epitaxial layers of $Si_{1-x}Sn_x$ solid solutions have been grown by bimolecular beam epitaxy [1], ion beam-assisted solid phase epitaxy [2], and liquid phase epitaxy from a tin-based solution melt [3]. There are studies on the phase diagrams of the Si–Sn and Ge–Sn systems [4, 5], local atomic structures of the $Ge_{1-x}Sn_x$ and $Si_{1-x}Sn_x$ solid solutions [6], quantum dots in the $Ge_{1-x}Sn_x$/Ge and $Si_{1-x}Sn_x$/Si alloys [7], growth mechanisms of Sn quantum dots in the Si matrix [8], and optical properties of diamond-like substitutional solid solutions of the compositions $Ge_{1-x}Si_x$, $Ge_{1-x}Sn_x$, $Si_{1-x}Sn_x$, and $Si_{1-x}C_x$ [9]. The prospects for the use of these solid solutions have been demonstrated in stud-

ies of their physical properties and fabrication technologies.

The purpose of this work was to grow films of the $Si_{1-x}Sn_x$ ($0 \le x \le 0.04$) solid solutions on a silicon substrate by liquid phase epitaxy and to investigate the structural quality of this material and the electrophysical properties of the related heterostructures p-Si$-n$-$Si_{1-x}Sn_x$ ($0 \le x \le 0.04$).

2. GROWTH OF THE SOLID SOLUTIONS $Si_{1-x}Sn_x$ ($0 \le x \le 0.04$)

Our approach to the study of the possibility of forming substitutional solid solutions based on Si and Sn is associated with the creation of conditions providing the formation of continuous substitutional solid solutions and is founded on the molecular-statistical and crystal-chemical concepts. The description of these conditions was proposed in [10, 11] as follows:

$$\Delta z = \sum_{i=1}^{m} z_i^m - \sum_{i=1}^{n} z_i^n = 0, \qquad (1)$$

$$\Delta r = \left| \sum_{i=1}^{m} r_i^m - \sum_{i=1}^{n} r_i^n \right| \le 0.1 \sum_{i=1}^{m} r_i^m, \qquad (2)$$

where z_i^m and z_i^n are the valences and r_i^m and r_i^n are the covalent radii of atoms of chemical elements of the solvent m and the solute n or chemical elements that form molecules of the solvent and solute compounds, respectively, $i = 1, 2, 3, 4$. Condition (1) provides the electroneutrality of solute chemical elements or solute compounds in a solvent semiconductor material. This condition is satisfied when the solute chemical elements are isovalent to the chemical elements of the solvent semiconductor material. Condition (2) implies that the geometric parameters of the solvent m and the solute n are close to each other, which precludes the occurrence of significant distortions of the crystal lattice in the solid solutions. The smaller the parameter Δr, the lower the energy of elastic distortions of the crystal lattice and, therefore, the higher the degree of crystalline perfection of the solid solution and the higher the solubility of the solute n in the solvent m. When the difference between the sums of the covalent radii of atoms involved in the molecules forming the solid solution is more than 10%, the amount of a formed substitutional solid solution of these components is negligible.

As is known, silicon and tin are isovalent elements and satisfy the electroneutrality condition (1): $z_{Si} = z_{Sn}$. Figure 1 shows tetrahedral bonds between atoms in the $Si_{1-x}Sn_x$ solid solution. It can be seen from this figure that, in the crystal lattice of the solid solution, there are Si$-$Sn and Si$-$Si covalent bonds. The differ-
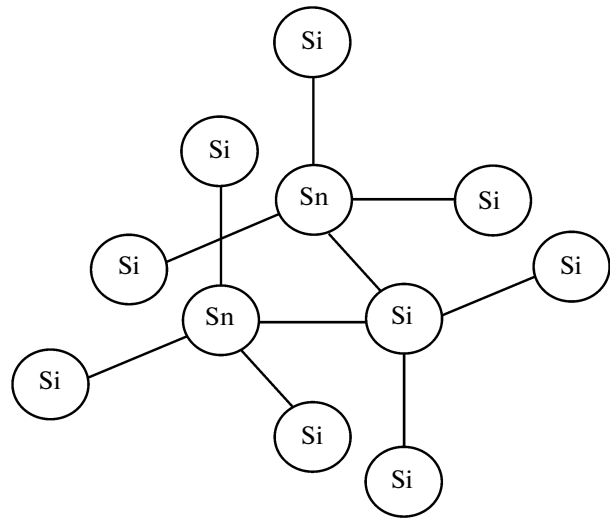

Fig. 1. Spatial configuration of the tetrahedral bonds between atoms of the $Si_{1-x}Sn_x$ solid solution.

ence between the sums of the covalent radii of atoms forming these bonds is 9.8%,

$$\Delta r = \left| (r_{Si} + r_{Si}) - (r_{Si} + r_{Sn}) \right| = 0.23 \,\text{Å}. \qquad (3)$$

Therefore, the covalent radii of atoms satisfy the condition of formation of a substitutional solid solution (2), and the $Si_{1-x}Sn_x$ compound is a stable phase. The substitution of the tin atoms for the silicon atoms leads only to a slight distortion of the crystal lattice; however, there can arise local microstresses of the growth nature with a low energy of elastic distortions of the crystal lattice.

The $Si_{1-x}Sn_x$ solid solutions were grown on a technological facility with a vertically installed quartz reactor. Horizontal Si substrates separated from each other by graphite supports were mounted in a graphite cassette of the reactor. A liquid tin solution melt was poured through side slits of the cassette into the space between two (upper and lower) substrates. The distance between the upper and lower substrates was varied in the range from $0.25-2.50$ mm by using the properly selected graphite supports of different thicknesses. By this means, we could control the volume of the liquid solution melt. Perfect crystalline epitaxial layers with mirror-smooth surfaces and best structural parameters were grown under the conditions where the distance between the upper and lower substrate was equal to 1 mm and the rate of forced cooling of the substrate was 1°C/min. The substrates were cut from single-crystal silicon in the form of disks with a (111) crystallographic orientation, a diameter of 20 mm, and a thickness of ~400 μm.

The solid solutions were grown from the Sn$-$Si solution melt. For this purpose, we investigated the solubility of silicon in tin. At temperatures below 700°C, the solubility of silicon in tin is relatively low; i.e., it is less than 0.4 at %. With an increase in the tem-

perature to 1000°C, the solubility of silicon in tin slowly increases and reaches a value of 2.2 at %. In the temperature range from 1000 to 1100°C, the solubility of silicon increases more rapidly and reaches a value of 9 at %. Therefore, it is desirable to perform the epitaxy process at relatively high temperatures (above 1000°C), at which the solubility of silicon is higher than 2 at %. Based on the thermodynamic conditions of growth of the solid solution, we carried out the epitaxy process at different temperatures of the onset of crystallization (900–1100°C). As a result, the optimum temperature of the onset of crystallization was found to be 1050°C.

The grown films had the n-type conductivity. The concentration of free charge carriers was 10^{17} cm^{-3}, and the Hall mobility of majority charge carriers at room temperature was ~538 cm^2/(V s). The thickness of the grown epitaxial layers varied in the range from 3 to 50 μm depending on the parameters of the technological process.

3. SAMPLE PREPARATION AND MEASUREMENT TECHNIQUES

For our investigations, the p-Si–n-Si$_{1-x}$Sn$_x$ heterostructures were fabricated by growing an epitaxial layer of the Si$_{1-x}$Sn$_x$ ($0 \leq x \leq 0.04$) solid solutions with the n-type conductivity and electrical resistivity of ~0.8 Ω cm on silicon substrates with the p-type conductivity and electrical resistivity of ~1 Ω cm. The structural investigations and measurements of the current–voltage characteristics were carried out using samples in which the epitaxial layer of the solid solution had a thickness of ~20 μm, whereas the spectral dependences of the photocurrent were studied using samples with the epitaxial layer ~40 μm thick. Ohmic current-collecting contacts (continuous on the back side and tetragonal with an area of 9 mm^2 on the side of the epitaxial layer) were prepared through vacuum deposition (~10^{-5} Torr) of silver.

The chemical composition of the surface and cleavage of an epitaxial layer of the Si$_{1-x}$Sn$_x$ solid solutions was determined using an X-ray microanalysis on a JEOL Model JSM-5910LV scanning electron microscope (Japan). The structural investigations on the side of the substrate and the film were carried out at a temperature of 300 K on a DRON-3M X-ray diffractometer (CuK_α radiation, λ = 0.15418 nm, ω–2θ scan mode) using step-by-step scanning with a monochromator of the perfect silicon crystal (the (111) reflection, FWHM = 6.2″) (FWHM is the full width at half-maximum).

The current–voltage characteristics of the p-Si–n-Si$_{1-x}$Sn$_x$ ($0 \leq x \leq 0.04$) heterostructures were measured in the dark at different temperatures (293–453 K) in the forward and reverse directions of the electric current at bias voltages in the range from −3 to +3 V. For this purpose, the samples were mechanically

firmly fixed on a metallic cryostat, which was heated and evacuated to a residual pressure of ~10^{-3} Torr. The temperature of the sample was measured with a calibrated chromel–copel thermocouple.

The voltage applied to the sample from a B5-45A power supply was measured with a V7-9 voltmeter. The electric current passing through a semiconductor structure was measured using an ShCh-300 combined digital device.

The spectral dependence of the photocurrent was measured on a facility with quartz optics and a prism monochromator (Carl Zeiss Jena, Germany) at room temperature. The measuring part of the facility and the sample were placed in a metallic box, which was shielded from external noise and illumination. The radiation source was a DKSSh-1000 xenon lamp operating in the minimum permissible power mode, which ensured a luminous flux of 53000 lm and a brightness up to 12×10^3 cd/m^2 at the center of the light spot. The radiation from the lamp at different wavelengths was calibrated to a single photon energy using a PTH-10C thermocouple with a quartz window, a detector element with an active area of 1×3 mm, and a sensitivity of 0.98 V/W. The photocurrent of the studied structures was measured with an F-116/2 microammeter.

4. EXPERIMENTAL RESULTS AND DISCUSSION

4.1. Structural Investigations of the Solid Solutions Si$_{1-x}$Sn$_x$ ($0 \leq x \leq 0.04$)

The performed analysis of the X-ray scanning images of the surface and cleavage of the epitaxial layer of the Si$_{1-x}$Sn$_x$ solid solution has demonstrated that the distribution of the components over the surface is homogeneous, whereas the tin content monotonically varies throughout the thickness of the film in the range $0 \leq x \leq 0.04$. A gradual increase in the molar content of tin throughout the thickness of the epitaxial layer reduces elastic stresses generated as a result of the mismatch between the lattice parameters of the substrate and the film.

Figure 2a shows the X-ray diffraction pattern of the single-crystal silicon substrate, which contains several structural reflections of the selective character above the inelastic background: the intense line (111)$_{Si}$ with $d_0/n = 0.3128$ nm and the low-intensity line (222)$_{Si}$ with $d_0/n = 0.1546$ nm (where d_0 is the interplanar distance and n is the serial number of the plane). The (222) reflection is a second-order satellite reflection of the main reflection (111), and the β component of the main reflection is observed at the scattering angle 2θ = 25.83°. The small width (FWHM = 0.0032 rad), maximum intensity (4×10^5 imp/s), and good splitting of the (111) reflection in the α_1 and α_2 radiations, for which the intensity ratios of the components are close to the calculated intensity ratio $I(\alpha_1) = 2I(\alpha_2)$, suggest

a high degree of perfection of the crystal lattice of the substrate (see inset to Fig. 2a). However, the (222) reflection in the X-ray diffraction pattern of the substrate is "forbidden" by the selection rules and should not exist in the equilibrium lattice of silicon [12]. The ratio of the intensity of this reflection to the intensity of the main reflection is $I(222)/I(111) \approx 7 \times 10^{-4}$; i.e., it is greater than the value of 10^{-4}, which corresponds to the upper limit of the statistical (homogeneous) distribution of the solute (oxygen) atoms in the lattice of the solvent (silicon) [13]. This circumstance indicates the presence of precipitates (inclusions) of oxygen in silicon in the amorphous (SiO_x) and crystalline (SiO_2) modifications of the growth character in local imperfect regions of the matrix lattice. The broad diffuse reflection with $d_0/n = 0.5539$ nm ($2\theta = 16°$) is attributed to the presence of SiO_2 amorphous nanoparticles with a size of ~1 nm on the surface, while the weak selective line with $d_0/n = 0.2468$ nm ($2\theta = 36.6°$) corresponds to diffraction reflections from the {110} plane of nanoinclusions with the SiO_2 crystal lattice in the bulk of the substrate at the interface between the blocks. The amorphous layer on the silicon surface was newly formed with time, because, during the preparation of the film, it was removed by the chemical etching. The size of nanoinclusions was determined from the width of the (110) reflection according to the Selyakov−Scherrer formula ($L = 0.94\lambda/(\omega\cos\theta)$, where λ is the radiation wavelength, ω is the half-width of the reflection, and θ is the Bragg angle) and reached ~9 nm. The ratio of the specific volumes of the unit cells is equal to $V(SiO_2)/V(Si) \approx 2$. This means that the stored elastic energy, which is associated with the local ultimate distortion of the Si matrix lattice due to the inhomogeneous distribution of oxygen, is consumed in the formation of quartz nanoinclusions in the bulk of the substrate. As a result of this process, the X-ray diffraction pattern exhibits a "forbidden" reflection (222) from the silicon lattice. The weak intensity of this reflection indicates that a small local distortion of the matrix lattice around the formed quartz nanocrystals is retained. If quartz nanocrystals were to be not formed, the ultimate distortion of the matrix lattice should lead to an ultimate broadening of the main reflection (111), which should be multiple of the increase in the intensity of the forbidden reflection (222), as well as to a significant modulation of the level of the inelastic background. However, the background is smooth and corresponds to an almost undistorted lattice (Fig. 2a).

Figure 2b shows the X-ray diffraction pattern of the epitaxial layer of the $Si_{1-x}Sn_x$ solid solution, which differs significantly from the X-ray diffraction pattern of the substrate (Fig. 2a). The performed analysis of the X-ray diffraction pattern has demonstrated that the most intense selective reflection $(111)_{Si}$ with $d_0/n = 0.3143$ nm ($2\theta = 28.42°$) is associated with the scattering of X-rays from the {111} basal planes of the
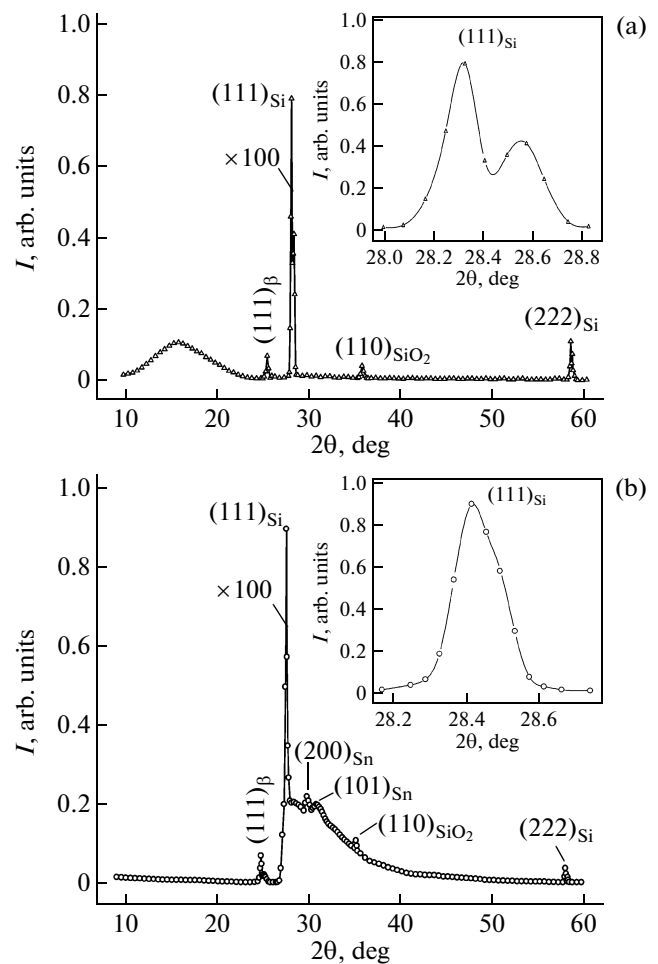

Fig. 2. X-ray diffraction patterns of (a) Si substrate and (b) $Si_{0.96}Sn_{0.04}$ epitaxial solid solution. Insets show the shapes of the structural reflection $(111)_{Si}$ on an enlarged scale for (a) Si substrate and (b) $Si_{1-x}Sn_x$ solid solution.

silicon sublattice of the film and has FWHM $\approx$ 0.0027 rad. For this reflection, the β component $(111)_\beta$ is observed at the scattering angle $2\theta = 25.67°$. The intensity of the main reflection (111) of the film is 13% higher than the intensity of this line for the substrate. This suggests a partial replacement of the silicon ions by the isovalent tin ions in the film, because the X-ray scattering intensity is proportional to the atomic number (z) of the elements. The small width of the main peak $(111)_{Si}$ indicates a high degree of perfection of the single-crystal lattice of the films with the (111) orientation. According to the estimates obtained from the width of this peak, the size of subgrains (blocks) in the film is approximately equal to 60 nm. However, this peak is a singlet without a splitting in the α_1 and α_2 radiations, even though there is a slight asymmetry in the wide-angle scattering range (see inset to Fig. 2b). This suggests that there are residual elastic microstresses of the growth nature in the film. The appearance of the forbidden reflection $(222)_{Si}$
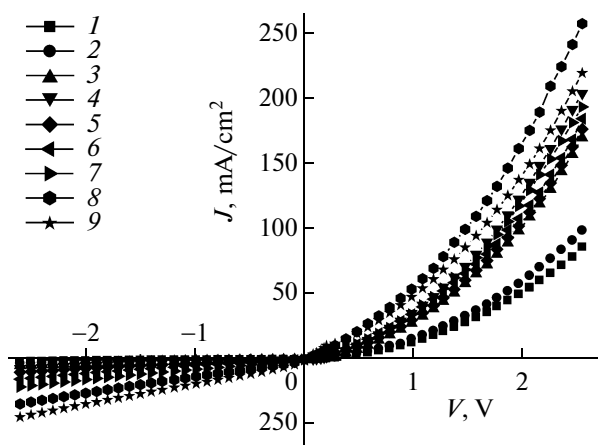
Fig. 3. Current–voltage characteristics of the p-Si–n-Si$_{1-x}$Sn$_x$ ($0 \leq x \leq 0.04$) heterostructure at different temperatures $T = $ (*1*) 293, (*2*) 313, (*3*) 333, (*4*) 353, (*5*) 373, (*6*) 393, (*7*) 413, (*8*) 433, and (*9*) 453 K.

with $d_0/n = 0.1570$ nm ($2\theta = 58.75°$) in the X-ray diffraction pattern and the intensity ratio $I(222)/I(111)_{Si} = 3.11 \times 10^{-4}$ indicate that the concentration of the α-SiO$_2$ phase in the film is more than two times lower than that in the silicon substrate. The absence of a diffuse reflection in the X-ray diffraction pattern suggests that the surface of the grown film does not contain SiO$_x$ amorphous precipitates. Therefore, it is reasonable to assume that the microdistortions revealed in the silicon sublattice of the film are caused by the difference in the ionic radii of silicon ($r_{Si}^{4+} = 0.42$ Å) and tin ($r_{Sn}^{4+} = 0.71$ Å) atoms located at the substitutional sites [14].

In addition, the gentle slope of the right wing of the (111) reflection profile indicates that the grown film contains defects of the stacking fault type. Furthermore, on the right wing of this reflection, there are also three clearly distinguished selective reflections with a weak intensity. One of them with $d_0/n = 0.2496$ nm ($2\theta = 36°$) is attributed to the scattering of X-rays from the (110) planes of the crystalline impurity phase α-SiO$_2$ with a characteristic crystallite size of 38 nm. The two other reflections are associated with the crystal lattice of the tin nanocrystals that are differently oriented with respect to the substrate. The broad (1.75×10^{-2} rad) reflection (101) with $d_0/n = 0.2797$ nm ($2\theta = 31.9°$) belongs to nanocrystallites of the tin phase with a size of 8 nm. The other, less broad (1.16×10^{-2} rad), peak (200) with $d/n = 0.2907$ nm ($2\theta = 30.7°$) also belongs to nanoparticles of this phase, but with a size of 12 nm. This circumstance indicates that the {101} and {200} crystallographic planes of particles of the precipitated tin phase are in coherent contact with the {111} planes of the silicon sublattice of the film. In this case, the interfaces between the substrate and tin nan-

oprecipitates will be more coherent, which can lead to an increase in the hardness of the grown film [15]. If the isovalent Sn ions were to be substituted for the Si ions in the matrix lattice of the film statistically (homogeneously), the X-ray diffraction pattern would contain no reflections from the Sn nanocrystals and only the intensity of the main reflection (111)$_{Si}$ and, possibly, even the intensity of the third-order satellite reflection (333) would be increased. However, we observe the opposite situation in the X-ray diffraction pattern: it contains selective reflections from Sn nanocrystals formed as a result of the segregation of the Sn ions in the local imperfect region of the Si sublattice of the film, for example, at the Si–SiO$_2$ interfaces and in near-the-boundary regions between the silicon blocks (subgrains) and the SiO$_2$ phases [16]. In these regions, there are lattice sites with a high potential owing to the unsaturated chemical bonds between the ions, and the substitution of the impurity tin ions for the matrix silicon ions occurs with a lower energy than in the lattice sites with a low potential in the bulk of the blocks with a regular structure and saturated bonds. The impurity tin ions are easily transported to the imperfect regions of the film by means of diffusion, because the rate of diffusion of these ions and their molecules in the interfaces between the phases and blocks is almost two orders of magnitude higher than the rate of bulk diffusion of the same ions [16]. This diffusion process promotes a rapid increase in the concentration of impurity ions up to a value necessary for the formation of tin nanocrystals in imperfect regions of the film. Another reason for the segregation of the tin ions at the interfaces between the phases and blocks is associated with the difference between the energies of interaction of the ions: $E(\text{Sn–Sn}) > E(\text{Si–Sn})$ and $E(\text{Sn–Sn}) > E(\text{Si–Si})$.

Furthermore, there is a significant difference in the parameters of the silicon lattice of the substrate and the film. These parameters were determined in the direction perpendicular to the layer plane for the (200) and (400) structural lines with the use of the Nelson–Riley function $1/2(\cos^2\theta/\sin\theta + \cos^2\theta/\theta)$ extrapolated to $\theta = 90°$ [12]. The lattice parameters of the film (a_f) and the substrate (a_s) are respectively as follows: $a_f = 0.54383$ nm and $a_s = 0.54342$ nm. The mismatch of the lattice constants $\xi = 2|a_s - a_f|/(a_s + a_f) = 0.0008$ satisfies the criterion for coherence of the interface between the phases. The accuracy in the determination of the interplanar distances and the lattice parameters was ~0.00001 nm. Tin has a body-centered tetragonal crystal lattice, which is characterized by two unit cell parameters, namely, a and c. These parameters are determined using the selective reflections (200) and (101) belonging to the tin nanocrystallites as $a_{Sn} = 0.5838$ nm and $c_{Sn} = 0.3186$ nm, which are close to the tabular data $a_{Sn} = 0.5831$ nm and $c_{Sn} = 0.3182$ nm [12].

4.2. Current−Voltage Characteristics of the Heterostructures p-Si−n-Si$_{1-x}$Sn$_x$ ($0 \leq x \leq 0.04$) at Different Temperatures

The current−voltage characteristics shown in Fig. 3 were measured in the dark at temperatures in the range from 293 to 453 K. The performed investigations demonstrated that, with an increase in the temperature, the current density J increases in both the forward and reverse directions of the current, but the relationship $J = f(V)$ remains valid for all temperatures. The initial part of the current−voltage characteristics (up to 0.2 V) is adequately described by the exponential dependence derived by Stafeev [17], which is characteristic of the so-called "long" p−n structure diode (i.e., when $d/L_p > 1$, where d is the length of the base and L_p is the diffusion length of minority charge carriers) and which was improved later in [18] for the p−i−n structures:

$$J = J_0 \exp\left(\frac{qV}{ckT}\right), \qquad (4)$$

$$c = \frac{2b + \cosh(d/L_p) + 1}{b + 1}, \qquad (5)$$

where $b = \mu_n/\mu_p$ is the ratio of the electron mobility μ_n to the hole mobility μ_p. The values of the factor c in the exponent and the pre-exponential factor J_0 calculated from the data on the current−voltage characteristics at different temperatures are presented in the table.

The mobility of majority charge carriers, i.e., electrons, was determined using the Hall method and, at room temperature, reached $\mu_n \approx 538$ cm^2/(V s). Under the assumption that, in IV semiconductor materials, as usual, the hole mobility is not much less than the electron mobility, the mobility ratio used for the estimation was taken as $b = 3$ [19]. The thickness of the high-resistivity base n-Si$_{1-x}$Sn$_x$ was $d \approx 20$ μm. Knowing the values of the factor c from formula (5), we can find the ratio $d/L_p = 2.1$, which is actually larger than unity. Then, we can find the value of L_p, which at 293 K proved to be $L_p \approx 9.57$ μm. This allows us to determine the product of the mobility by the lifetime of minority charge carriers $\mu_p\tau_p = qL_p^2/kT$. The values of this product for different temperatures are presented in the table. It can be seen from the table that, with an increase in the temperature, the product $\mu_p\tau_p$ weakly depends on the temperature in the range from 293 to 333 K and, then, up to 453 K, decreases. The analysis of these data has demonstrated that, in the temperature range from 333 to 433 K, the dependence $\mu_p\tau_p = f(1/T^{3/2})$ has a linear behavior. The temperature dependence of the quantity $\mu_p\tau_p$ suggests that thermal vibrations of the crystal lattice play an important role in the scattering mechanism of charge carriers.

Values of the factor c in the exponent and the pre-exponential factor J_0 in formula (4), the product of the mobility by the lifetime of minority charge carriers $\mu_p\tau_p$, the electrical resistivity ρ of the high-resistivity layer of the n-Si$_{1-x}$Sn$_x$ solid solution according to the calculation from the exponential segment of the experimental current−voltage characteristics at different temperatures

T, K	c	J_0, μA/cm^2	$\mu_p\tau_p$, 10^{-5} cm^2/V	ρ, 10^5 Ω cm
293	2.78	41	3.62	5.74
313	2.77	63	3.41	3.95
333	2.66	110	3.62	2.32
353	2.62	176	3.57	1.50
373	2.85	286	2.66	1.06
393	2.93	471	2.37	0.69
413	3.23	720	1.86	0.47
433	3.13	1373	1.86	0.26
453	3.18	2043	1.75	0.18

The pre-exponential factor in formula (4) is described by the expression [17]

$$J_0 = \frac{kTb\cosh(d/L_p)}{2q(b+1)L_p\rho\tan(d/2L_p)}, \qquad (6)$$

where k is the Boltzmann constant, T is the absolute temperature, q is the elementary charge, and ρ is the electrical resistivity of the high-resistivity base. Using expression (6), we found the values of the electrical resistivity at different temperatures. These values are presented in the table. It can be seen that an intermediate layer of the solid solution with a high electrical resistivity is formed between the substrate and the epitaxial film. The electrical resistivity of the epitaxial film was determined using the Hall method and, at room temperature, reached ~0.8 Ω cm; therefore, the structure under investigation can be considered as a junction p-Si−n-Si$_{1-x}$Sn$_x$−n^+-Si$_{1-x}$Sn$_x$ ($0 \leq x \leq 0.04$) with a high-resistivity base n-Si$_{1-x}$Sn$_x$.

As is known, the electrical resistivity at a given temperature is determined by the concentration of majority charge carriers n, i.e., $\rho = 1/q\mu_n n$. Taking into account the scattering of charge carriers by thermal lattice vibrations and using the data presented in the table, we plotted the temperature dependence of the concentration of majority charge carriers n (Fig. 4a) for the high-resistivity base n-Si$_{1-x}$Sn$_x$. It can be seen from Fig. 4a that the concentration of free charge carriers in the high-resistivity layer at 293 K has the value of ~2×10^{10} cm^{-3}; with an increase in the temperature, it increases and, at 453 K, reaches ~1×10^{12} cm^{-3}. Hence, it follows that the intermediate layer n-Si$_{1-x}$Sn$_x$ formed between the substrate p-Si and the epitaxial film n^+-Si$_{1-x}$Sn$_x$ ($0 \leq x \leq 0.04$) is a highly
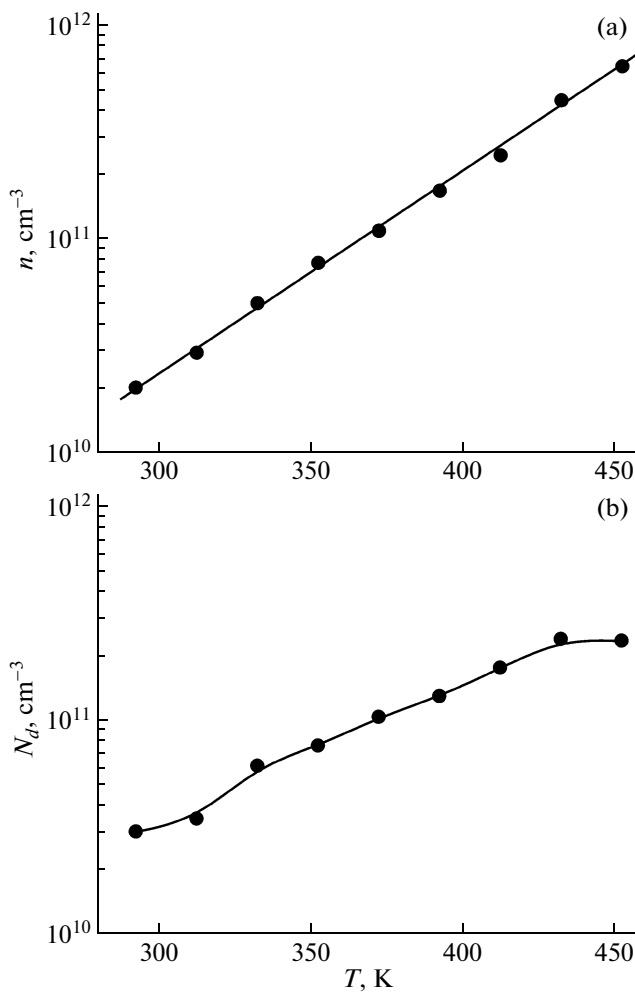
Fig. 4. Dependences of the concentrations of (a) majority charge carriers n and (b) uncompensated donor centers N_d on the temperature of the high-resistivity layer of the n-$Si_{1-x}Sn_x$ solid solution.

compensated material, which primarily determines the electronic processes occurring in the structure as a whole, including the charge carrier transport mechanism. The calculation of the concentration of majority charge carriers from the calculated electrical resistivity gives an average estimate. The calculated points (Fig. 4a) plotted on a semilogarithmic scale lie on a straight line; i.e., the dependence $n = f(T)$ has an exponential behavior, which, most likely, indicates a homogeneous distribution of impurities in the solid solution under investigation.

In all the current−voltage characteristics shown in Fig. 3, the exponential portion transforms into the power-law portion of the voltage dependence of the current in the form $J \sim V^2$. When the applied voltage reaches ~2 V, the electric field at the base of the studied structure becomes one order of magnitude stronger than the field in the initial exponential part of the current−voltage characteristic (in the voltage range $V <$

0.2 V). Consequently, in the square-law portion of the current−voltage characteristic, the diffusion term can be disregarded; then, the electric current is predominantly determined by the drift component. On this basis, the square-law portion of the current−voltage characteristic can be described by the drift mechanism of charge carrier transport in the electrical resistance relaxation mode, which is realized when the injected space charge is less than the charge of uncompensated donors N_d. In this case, the basic equation describing the change in the free charge carrier concentration n has the form [20]

$$\frac{JN_d}{q(b+1)^2 n^2}\frac{dn}{dx} + U = 0, \tag{7}$$

where U is the recombination rate of nonequilibrium charge carriers.

Equation (7) is solved under conditions of nonideality of injecting contacts, i.e., when the concentrations of free charge carriers in the $p-n$ and $n-n^+$ junctions are determined as $n(0) \propto \sqrt{J}$ and $n(d) \propto \sqrt{J}$, respectively. Under these conditions, the electric current through the $p-n$ junction is provided not only by the purely hole component but also by the electron component. Similarly, the electric current through the $n-n^+$ junction is determined not only by the purely electron component but also by the hole component. Under these conditions, the solution to equation (7) gives the following form of the current−voltage characteristic [21]:

$$J = \frac{9}{8}\frac{q\mu_p\tau_p\mu_n N_d}{d^3}V^2. \tag{8}$$

Using expression (8) and the data presented in the table, from the square-law portion of the current−voltage characteristic, we obtained the dependence $N_d = f(T)$, which is shown in Fig. 4b. It can be seen from this figure that, with an increase in the temperature, the concentration of uncompensated donors in the high-resistivity layer n-$Si_{1-x}Sn_x$ increases from $N_d \approx 3 \times 10^{10}$ cm^{-3} at room temperature to $N_d \approx 2.4 \times 10^{11}$ cm^{-3} at 453 K.

The temperature dependence of the concentration N_s shows that the levels of donor impurities in the n-$Si_{1-x}Sn_x$ solid solution are arranged almost continuously in energy, and their concentration increases as the middle of the band gap is approached.

4.3. Spectral Dependence of the Photocurrent of the Heterostructures p-Si−n-$Si_{1-x}Sn_x$ $(0 \le x \le 0.04)$

We investigated the spectral dependences of the short-circuit photocurrent of the p-Si−n-$Si_{1-x}Sn_x$ $(0 \le x \le 0.04)$ heterostructures and control samples— the conventional silicon structures p-Si−n-Si without

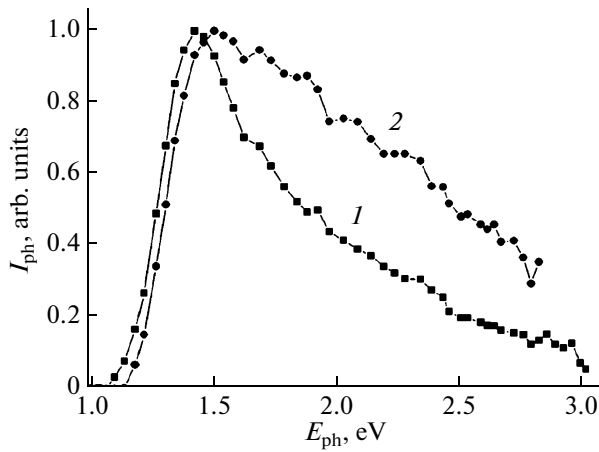**Fig. 5.** Spectral dependences of the photocurrent in the structures (*1*) p-Si$-n$-Si$_{1-x}$Sn$_x$ ($0 \leq x \leq 0.04$) and (*2*) p-Si$-n$-Si.

Sn impurities—over a wide spectral range of photon energies E_{ph}. In order to provide a complete absorption by the Si$_{1-x}$Sn$_x$ solid solution over a wide range of the emission spectrum, we fabricated p-Si$-n$-Si$_{1-x}$Sn$_x$ heterostructures with n-Si$_{1-x}$Sn$_x$ ($0 \leq x \leq 0.04$) epitaxial layers of sufficient thickness ($d \approx 45 \ \mu$m).

The spectral dependences of the photocurrent of the structures under investigation are shown in Fig. 5. As can be seen from this figure, the spectral region of photosensitivity of the p-Si$-n$-Si$_{1-x}$Sn$_x$ ($0 \leq x \leq 0.04$) heterostructures covers the wide range of photon energies from 1.06 to 3.00 eV (curve *1* in Fig. 5) and is shifted toward longer wavelengths by the value $\Delta E \approx 0.06$ eV as compared to the control structure (curve *2* in Fig. 5). The shift in the photosensitivity of the studied structures toward the long-wavelength range is determined by the band gap of the Si$_{1-x}$Sn$_x$ ($0 \leq x \leq 0.04$) solid solution. From the shift in the photosensitivity, we estimated the band gap $E_{g, \mathrm{SiSn}}$ of the Si$_{1-x}$Sn$_x$ ($0 \leq x \leq 0.04$) solid solution, which at room temperature is equal to $E_{g, \mathrm{SiSn}} = E_{g, \mathrm{Si}} - \Delta E = 1.06$ eV, where $E_{g, \mathrm{Si}} = 1.12$ eV is the band gap of single-crystal silicon.

A decrease in the photocurrent of the studied structures in the short-wavelength region of the radiation spectrum is determined by the location depth of the separating $p-n$ junction; in our case, it is equal to 45 μm. When the diffusion length of minority charge carriers is less than the location depth of the separating barrier, electron–hole pairs generated by high-energy photons in the near-surface region of the structure do not reach the separating barrier and, hence, do not participate in the generation of the photocurrent, which leads to a decrease in the photocurrent of the studied structure in the short-wavelength region of the spectrum. However, our purpose was to design and synthesize a material that would provide a higher sensitivity in the long-wavelength region as compared to conventional silicon structures, which is seen in Fig. 5.

5. CONCLUSIONS

Thus, the Si$_{1-x}$Sn$_x$ ($0 \leq x \leq 0.04$) solid solutions grown by liquid phase epitaxy have a perfect single-crystal structure with a (111) crystallographic orientation and a subgrain size of 60 nm. The tin ions substitute for the silicon ions in the crystal lattice of the film statistically heterogeneously and undergo segregation in imperfect regions of the film, or, more precisely, at the interfaces between the Si blocks and phases (SiO$_2$ nanocrystals with a size of 38 nm) and in the near-the-boundary regions of the crystal lattice of the film. The lattice mismatch between the film $a_f = 0.54383$ nm and the substrate $a_s = 0.54342$ nm amounts to $\xi = 2|a_s - a_f|/(a_s + a_f) = 0.0008$, which satisfies the criterion for coherence of the interface.

During liquid phase epitaxy of the solid solution, in the region between the p-Si substrate and the n-Si$_{1-x}$Sn$_x$ ($0 \leq x \leq 0.04$) epitaxial film there arises a compensated high-resistivity layer with an electrical resistivity of $5.74 \times 10^5 \ \Omega$ cm at room temperature. With an increase in the temperature, the concentration of free charge carriers in the high-resistivity layer increases according to the exponential law. Levels of donor impurities in the n-Si$_{1-x}$Sn$_x$ solid solution are arranged almost continuously in energy, and their concentration increases as the middle of the band gap is approached.

The photosensitivity of the p-Si$-n$-Si$_{1-x}$Sn$_x$ ($0 \leq x \leq 0.04$) heterostructure embraces the spectral range of photon energies from 1.06 to 3.00 eV and is shifted toward longer wavelengths as compared to the photosensitivity of conventional silicon structures p-Si$-n$-Si.

The grown solid solutions Si$_{1-x}$Sn$_x$ ($0 \leq x \leq 0.04$) can be used as an active element for the design and fabrication of optoelectronic devices operating in the infrared region of the radiation spectrum.

It should, however, be noted that, for the widespread use of this solid solution as an active element of optoelectronic devices, it is necessary to extend the spectral region of sensitivity in the long-wavelength range, which, in turn, requires the use of solid solutions with a higher tin content. The solution of this problem should be the subject of further investigation.

REFERENCES

1. M. F. Fyhn, J. Lundsgaard Hansen, J. Chevallier, and A. Nylandsted Larsen, Appl. Phys. A: Mater. Sci. Process. **68** (2), 259 (1999).
2. N. Kobayashi, M. Hasegawa, H. Hayashi, H. Katsumata, Y. Makita, H. Shibata, and S. Uekusa, Mater. Res. Soc. Symp. Proc. **396**, 207 (1996).

3. B. Sapaev and A. S. Saidov, Tech. Phys. Lett. **29** (11), 963 (2003).

4. T. Soma and S. Kagaya, Phys. Status Solidi B **105**, 311 (1981).

5. T. Soma, K. Kamada, and H. Matsuo Kagaya, Phys. Status Solidi B **147**, 109 (1988).

6. V. G. Deibuk and Yu. G. Korolyuk, Semicond. Phys. Quantum Electron. Optoelectron. **8** (1), 1 (2005).

7. R. Ragan, K. S. Min, and H. A. Atwater, Mater. Sci. Eng., B **87**, 204 (2001).

8. P. Möck, Y. Lei, T. Topuria, N. D. Browning, R. Ragan, K. S. Min, and H. A. Atwater, Mater. Res. Soc. Symp. Proc. **770**, 1 (2003).

9. Yu. G. Korolyuk, V. G. Deibuk, and Ya. I. Vyklyuk, Zh. Fiz. Dosl. **8** (1), 77 (2004).

10. M. S. Saidov, Geliotekhnika, No. 5, 48 (1997).

11. M. S. Saidov, Geliotekhnika, No. 3, 52 (1999).

12. S. S. Gorelik, L. N. Rastorguev, and Yu. A. Skakov, *X-Ray and Electron-Optical Analysis* (Metallurgiya, Moscow, 1970) [in Russian].

13. I. L. Shul'pina, R. N. Kyutt, V. V. Ratnikov, I. A. Pro-khorov, I. Zh. Bezbax, and M. P. Shcheglov, Tech. Phys., **55** (4), 537 (2010).

14. *Brief Reference Book of Physico-Chemical Quantities*, Ed. by A. A. Ravdel' and A. M. Ponomapeva (Khimiya, Leningrad, 1983) [in Russian].

15. A. M. Krivtsov and N. F. Morozov, Phys. Solid State **44** (12), 2260 (2002).

16. B. C. Bokshtein, C. Z. Bokshtein, and A. A. Zhukho-vitskii, *Thermodynamics and Kinetics of Diffusion in Solids* (Metallurgiya, Moscow, 1975; Oxonian, New Delhi, 1985).

17. V. I. Stafeev, Sov. Phys. Tech. Phys. **3**, 1502 (1958).

18. E. I. Adirovich, P. M. Karageorgii-Alkalaev, and A. Yu. Leiderman, *Double Injection Currents in Semiconductors* (Sovetskoe Radio, Moscow, 1978) [in Russian].

19. K. V. Shalimova, *Physics of Semiconductors* (Energoat-omizdat, Moscow, 1985) [in Russian].

20. A. Yu. Leidepman and M. K. Minbaeva, Semiconductors **30** (10), 905 (1996).

21. M. Lampert and P. Mark, *Current Injection in Solids* (Academic, New York, 1970; Mir, Moscow, 1973).

Translated by O. Borovik-Romanova

SPELL: OK